Longitudinal Detection of Optic Nerve Head Changes by Spectral Domain Optical Coherence Tomography in Early Experimental Glaucoma

Lin He,[1] Hongli Yang,[1,2] Stuart K. Gardiner,[2] Galen Williams,[1] Christy Hardin,[1] Nicholas G. Strouthidis,[3] Brad Fortune,[2] and Claude F. Burgoyne[1,2]

[1]Optic Nerve Head Research Laboratory, Devers Eye Institute, Legacy Health, Portland, Oregon
[2]Discoveries in Sight Research Laboratories of the Devers Eye Institute, Legacy Health, Portland, Oregon
[3]National Institute for Health Research Biomedical Research Centre at Moorfields Eye Hospital National Health Service Foundation Trust and University College London Institute of Ophthalmology, London, United Kingdom

Correspondence: Claude F. Burgoyne, Optic Nerve Head Research Laboratory, Devers Eye Institute, Legacy Research Institute, 1225 NE 2nd Avenue, PO Box 3950, Portland, OR 97208-3950; cfburgoyne@deverseye.org.

LH and HY contributed equally to the work presented here and should therefore be regarded as equivalent authors.

Submitted: September 11, 2013
Accepted: November 5, 2013

Citation: He L, Yang H, Gardiner SK, et al. Longitudinal detection of optic nerve head changes by spectral domain optical coherence tomography in early experimental glaucoma. *Invest Ophthalmol Vis Sci*. 2014;55:574–586. DOI:10.1167/iovs.13-13245

Purpose. We determined if the detection of spectral-domain optical coherence tomography (SDOCT) optic nerve head (ONH) change precedes the detection of confocal scanning laser tomography (CSLT) ONH surface, SDOCT retinal nerve fiber layer (RNFL), scanning laser perimetry (SLP), and multifocal electroretinography (mfERG) change in eight experimental glaucoma (EG) eyes.

Methods. Both eyes from eight monkeys were tested at least three times at baseline, and then every 2 weeks following laser-induced chronic unilateral IOP elevation. Event and trend-based definitions of onset in the control and EG eyes for 11 SDOCT neural and connective tissue, CSLT surface, SDOCT RNFL, SLP, and mfERG parameters were explored. The frequency and timing of onset for each parameter were compared using a logrank test.

Results. Maximum post-laser IOP was 18 to 42 mm Hg in the EG eyes and 12 to 20 mm Hg in the control eyes. For event- and trend-based analyses, onsets were achieved earliest and most frequently within the ONH neural and connective tissues using SDOCT, and at the ONH surface using CSLT. SDOCT ONH neural and connective tissue parameter change preceded or coincided with CSLT ONH surface change in most EG eyes. The SDOCT and SLP measures of RNFL thickness, and mfERG measures of visual function demonstrated similar onset rates, but occurred later than SDOCT ONH and CSLT surface change, and in fewer eyes.

Conclusions. SDOCT ONH change detection commonly precedes or coincides with CSLT ONH surface change detection, and consistently precedes RNFLT, SLP, and mfERG change detection in monkey experimental glaucoma.

Keywords: glaucoma, optic nerve head, lamina cribrosa, Bruch's membrane opening, retinal nerve fiber layer, optical coherence tomography

Glaucoma is an optic neuropathy that includes important pathophysiology within the brain, optic nerve, optic nerve head (ONH), and retina. In the monkey experimental glaucoma model, a substantial literature supports early injury to the retinal ganglion cell (RGC) axons within the ONH as a primary site of glaucomatous damage to the visual system.[1,2] Early ONH change includes not just neural, but also connective tissue components.[3,4] Therefore, detection of the neuropathy in monkeys at its onset should include structural and functional endpoints, and the structural endpoints should include neural and connective tissue targets.

Confocal scanning laser tomography (CSLT) has been used to detect surface height change of the ONH using algorithms, such as mean position of the disc (MPD)[5,6] and topographic change analysis (TCA).[7] Retinal nerve fiber layer thickness (RNFLT) and retardance can be measured by optical coherence tomography (OCT) and scanning laser polarimetry (SLP), respectively, to estimate RGC loss.[8–10] Functional abnormalities of the retina, including retinal ganglion cells in monkeys, can be detected by multifocal electroretinography (mfERG).[11,12] Emerging techniques, such as spectral domain OCT (SDOCT) are providing new insights into ONH disc margin, rim and laminar anatomy,[13–17] as well as new targets for the detection of the presence and progression of glaucomatous damage.[16,18,19] However, since experimental and clinical studies of the ONH using commercially available SDOCT only recently have become possible, to our knowledge there have been no longitudinal studies that have used SDOCT to characterize ONH change at the conversion of ocular hypertension to the onset of clinically detectible glaucomatous damage in monkeys or humans.

The monkey unilateral experimental glaucoma (EG) model produces an optic neuropathy that is indistinguishable from human glaucoma, though it is created over a shorter time course of months to years.[20] The model offers the unique opportunity to characterize and compare the sensitivity and specificity of ONH, and retinal structural and functional change detection within pre- and post-laser data sets from the control and EG eye of each animal.

Postmortem study of histomorphometrically reconstructed ONHs has identified five changes that define early monkey EG: (1) thickening[21] and (2) posterior displacement of the lamina cribrosa,[21] (3) expansion of the scleral canal,[22] (4) regional migration of the anterior and posterior laminar insertions from the sclera into the pial sheath,[30] and (5) thickening of the prelaminar neural tissue.[3] We previously reported the presence of SDOCT-detected deep ONH change at the time of CSLT ONH surface change within the pre-euthanasia SDOCT data sets of nine rhesus macaque monkeys with chronic, laser-induced, unilateral IOP elevations.[23] That study suggested several promising SDOCT parameters for assessing longitudinal change; however, it was limited by not using the complete set of baseline and post-laser imaging sessions preventing trend-based change detection, and did not make comparisons to SLP imaging and mfERG testing.

The primary purpose of our study was to test the hypothesis that the detection of SDOCT deep ONH change precedes the detection of CSLT ONH surface change, SLP retinal nerve fiber layer (RNFL) structural change, and mfERG retinal functional change in monkey EG. A second goal of this study was to evaluate the relative detectability for each testing modality and parameter within the data from the EG and control eyes.

Please see Supplementary Table S1 for a guide to the acronyms and abbreviations used within the text.

Methods

Animals

All experiments were performed in accordance with an institutionally-approved animal use protocol at Legacy Health, and conformed to the ARVO Animal Statement for the Use of Animals in Ophthalmic and Vision Research. Four young (<3 years old) and four old (>18 years old) rhesus monkeys (*Macaca mulatta*) were used in the current study.

Overall Experimental Design

Both eyes of each animal underwent CSLT, SDOCT, SLP, and mfERG testing on at least three occasions at baseline (prelaser; i.e., eyes normal). One eye of each monkey then was chosen randomly to receive 180° of argon laser photocoagulation to the trabecular meshwork so as to cause moderate, chronic IOP elevation.[24] A second 180° treatment was performed 2 weeks later. Post-laser imaging sessions in the lasered (hereafter referred to as the EG) eye and contralateral control eye continued in 1- to 3-week intervals. Laser photocoagulation was repeated in additional 90° increments as necessary to achieve and maintain IOP elevation. All animals were followed to the onset of CSLT-detected ONH surface change confirmed on two subsequent occasions in the EG eye.

CSLT and SDOCT Imaging Protocol

Animals initially were anesthetized with 15 mg/kg intramuscular ketamine and 0.2 mg/kg midazolam followed by a 0.05 mg/kg subcutaneous bolus of atropine sulfate. The monkeys then were intubated, and maintained on 100% oxygen and 1% to 2% isoflurane gas. Vital signs were monitored and maintained at normal ranges throughout all the experiments. Intravenous lactated Ringer's solution or 6% Hetastarch were administered to maintain blood pressure whenever mean arterial pressure fell below 65 mm Hg. One drop of topical 0.5% proparacaine was applied to each eye before a lid speculum was placed. The IOP was measured three times by applanation tonometry (Tonopen XL; Reichert, Inc., Depew, NY). Pupils then were dilated with 0.5% tropicamide and 2.5% phenylephrine before a plano rigid contact lens was placed on each eye with topical lubricant (0.5% carboxymethylcellulose sodium; Allergan, Inc., Irvine, CA) to keep the cornea moistened during the experiments.

A 27-gauge cannula was connected to a manometer and inserted through the temporal cornea into the anterior chamber. By adjusting the manometer, IOP was set at 10 mm Hg and stabilized for 30 minutes before CSLT and SDOCT imaging commenced, reducing or removing any reversible or conformational components of ONH deformation present from the eyes with elevated IOP that might cause acute conformational change, and capturing the manifestations of permanent glaucomatous ONH alternations. The ONH surface topography was measured by CSLT using a Heidelberg Retina Tomograph II (Heidelberg Engineering GmbH, Heidelberg, Germany).[25,26] A minimum of three individual scans were acquired at each CSLT imaging session and averaged to create a mean topography for each eye.

Eighty standard, nonenhanced depth imaging, 870 nm SDOCT (Spectralis; Heidelberg Engineering, GmbH) radial B-scans were acquired over a 15° area (768 A-scans per B-scan, $n = 9$ repetitions), followed by a 3.5 mm peripapillary RNFLT circle scan (1536 A-scans per B-scan, $n = 9$–16 repetitions). All repetitive scans were acquired using eye tracking (Spectralis Manual; Heidelberg Engineering GmbH) and averaged to reduce speckle noise. For each monkey eye, the center of the ONH was estimated and registered during the first imaging session, and was used to align all follow-up images.

mfERG Testing and SLP Imaging Protocol

The mfERG testing and SLP imaging were performed together under a separate protocol (so as to avoid anterior chamber needle placement), also every two weeks pre- and post-laser, but performed during the weeks between CSLT/SDOCT imaging sessions so as to alternate with them. For these sessions, general anesthesia was induced using ketamine (15 mg/kg intramuscular [IM]) in combination with either xylazine (0.8–1.5 mg/kg IM), along with a single subcutaneous injection of atropine sulphate (0.05 mg/kg). Animals then were intubated and breathed 100% oxygen for retinal function testing by electroretinography (ERG), during which anesthesia was maintained using a combination of ketamine (5 mg/kg/h intravenously) and xylazine (0.8 mg/kg/h IM). Upon completion of retinal function testing, ketamine-xylazine administration was discontinued and isoflurane gas (1%–2%) was mixed with oxygen to provide anesthesia during SLP scan acquisition.

Retinal function was evaluated by mfERG using VERIS (Electro-Diagnostic Imaging, Inc., Redwood City, CA) as described previously.[12] The mfERG stimulus consisted of 103 unscaled hexagonal elements subtending a total field size of approximately 55°. The luminance of each hexagon was modulated independently between "dark" (1 cd/m^2) and "light" (200 cd/m^2) according to a pseudorandom, binary m-sequence. Seven dark frames were inserted into each m-sequence step. Signals were amplified (gain = 100,000), band-pass filtered (10–300 Hz, with an additional 60-Hz line filter), sampled at 1.2 kHz (i.e., sampling interval = 0.83 ms), and digitally stored for subsequent off-line analyses. Two such recordings were obtained for each eye at each time point and averaged.

Peripapillary RNFL retardance measurements were obtained by SLP using a GDxVCC instrument (Carl Zeiss Meditec, Inc., Dublin, CA).[10] The instrument compensates for the effects of anterior segment (primarily corneal) birefringence to determine more accurately RNFL birefringence.[8] Thus, anterior segment birefringence measurements are obtained before

Investigative Ophthalmology & Visual Science

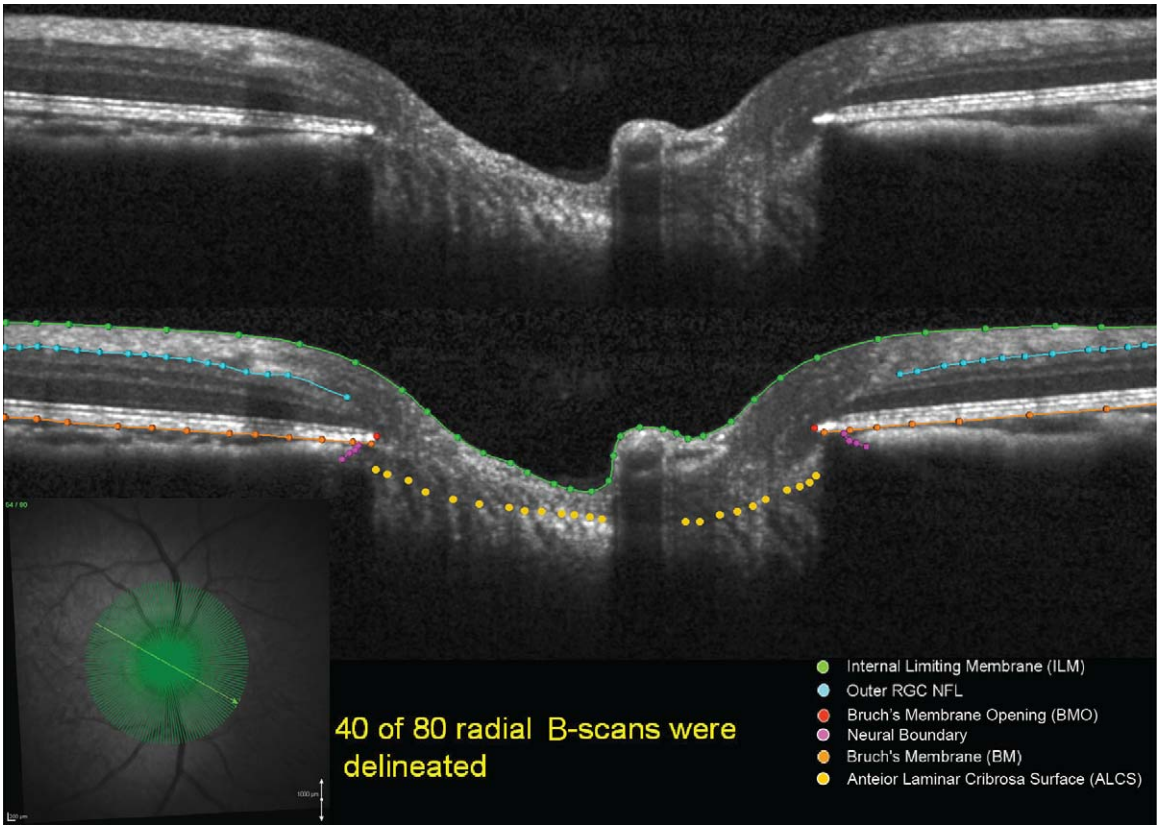

FIGURE 1. Original and delineated SDOCT ONH data sets in a normal monkey eye. One of two B-scans was delineated and, thus, yielded 40 delineated data sets for each monkey eye at a time. *Green lines/points*: ILM. *Blue lines/points*: outer boundary of the RNFL. *Orange lines/points*: BM/RPE. *Red points*: BMO. *Purple points*: BTE. *Yellow points*: ALCS.

initial baseline RNFL scans, then used to compensate all subsequent RNFL scans. A bite-bar, which rotates in three axes, was used to align the head and eye properly, and autorefraction was used for each scan. Three RNFL scans were averaged for each eye at each time point.

CSLT-Detected EG Onset

A trained technician outlined the optic disc margin within the baseline image of each eye using a disc photograph for reference where necessary; this contour line was transferred automatically to all subsequent images in the longitudinal series. For the current study, the parameter MPD was calculated for each CSLT session as described previously.[6] In this study, MPD was defined as the height of the surface of the ONH (i.e., average height of all pixels located within the disc margin contour line) relative to the height of a standard reference plane (a plane that runs parallel to the peripapillary retinal surface, and is set 50 μm below the retinal surface height at the papillomacular bundle, which is located in the −10° to −4° section temporal of the contour line, HRT II Operating Instructions, software version 1.6; Heidelberg Engineering GmbH). MPD onset was defined as the first post-laser session in which the MPD value was outside of the eye-specific 95% confidence interval (CI) determined by the baseline testing sessions, which then was confirmed in the two subsequent imaging sessions. Therefore, once three consecutive imaging sessions resulted in MPD outside the CI, the first of those three sessions was defined as MPD onset.

The TCA is a native change-detection algorithm embedded within the HRT II Explorer software package (Artes PH, et al. *IOVS* 2006;47:ARVO E-Abstract 4349). TCA onset was evaluated independently in each eye by two experienced investigators (CFB and BF)[12] masked to treatment condition (EG versus control) reading the TCA maps retrospectively. Change onset was defined as the first image showing ONH surface change exceeding baseline variability that was confirmed in the two subsequent sessions exceeding the magnitude and position of red TCA super-pixels within the $n = 5$ baseline imaging days. TCA onset at a given post-laser imaging session required a clinician to see similar TCA change in the two subsequent sessions. Where necessary, interobserver differences in TCA were adjudicated by the two readers through discussion.

For this study, EG onset was CSLT onset determined by either MPD or TCA, whichever was earlier. All monkeys were euthanized within 2 to 20 weeks after EG onset. Optic nerve axon counts for both eyes of each animal were performed using a previously-described automated segmentation algorithm that samples 100% of the optic nerve cross-section and counts 100% of the detected axons.[27]

SDOCT Data Set Delineation and Parameterization

Our methodology for delineation of SDOCT ONH data sets has been described in detail previously.[16,28,29] Customized "Multi-view" software (built on the Visualization Toolkit [VTK]; Kitware, Inc., Clifton Park, NY) was used to delineate the following anatomic features within 40 of the 80 radial B-scans (every other scan) of each SDOCT data set by two trained technicians who were masked to the treatment condition (EG or control eye) and timing (baseline or post-laser) of the data set (Fig. 1): internal limiting membrane (ILM), outer boundary of RNFL, Bruch's membrane/retinal pigment epithelium complex (BM/RPE), Bruch's membrane opening (BMO; inner-

most termination of the BM/RPE), border tissue of Elschnig (BTE; innermost termination of the choroid), and anterior lamina cribrosa surface (ALCS).

For the ILM, RNFL, BM/RPE, and BTE categories, each layer was delineated using discrete points interconnected by a Bézier curve. The position of each point in each category was finely adjusted, so that the fitted Bézier curve matched the feature of interest as closely as possible. BMO was delineated using two discrete points at either side of the neural canal. The ALCS was delineated based on our previous direct comparisons between SDOCT B-scans and matched histologic sections,[16,30] as well as our previous publications on SDOCT laminar visualization[16] and longitudinal change detection.[23] For each SDOCT B-scan data set, a point cloud including all the above landmarks was generated (Fig. 2). Because the Spectralis x,y transverse dimensions are calibrated for human eyes, a scaling factor of 0.857 was used to correct for ocular magnification differences in the monkey eye as described previously.[23]

To parameterize each SDOCT ONH data set, two reference planes were used. A BMO reference plane based on the best-fitting ellipse through the 80 delineated BMO points in a three-dimensional space (2 points/B-scan × 40 B-scans) and a BM reference plane based on the best-fitting ellipse through RPE/BM complex points located at a 1500 μm radius from the BMO centroid along the BMO plane. Eleven parameters from SDOCT ONH radial scan and 1 parameter from peripapillary circle scan were calculated and empirically categorized into ONH connective tissue, ONH neural tissue, and peripapillary RNFL groups as shown in Figure 2.

The ONH connective tissue parameters (Fig. 2A) included anterior laminar cribrosa surface depth (ALCSD) relative to BMO reference plane (ALCSD-BMO), ALCSD relative to BM reference plane (ALCSD-BM), BMO depth relative to the BM reference plane (BMOD-BM), and BMO area (BMOA). The ONH neural tissue parameters (Fig. 2B) included prelaminar tissue thickness (PLTT), minimum rim width (MRW),[23,29,31] rim volume (RimV), and cup volume (CupV). The RNFL parameters (Fig. 2C) included thickness calculated at eccentricities of 1200 and 1500 μm from the BMO centroid ($RNFLT_{1200}$ and $RNFLT_{1500}$), RNFL volume between eccentricities 1200 and 1500 μm (RNFLV), and RNFLT from the standard peripapillary retinal circle scan ($RNFLT_{circ}$).

mfERG Parameterization

From the average of the two recordings at each time point, a subset of local responses from the full array, limited to the central element and the three rings surrounding it (37 local responses in total), was processed to derive summary outcome parameters. A high-pass filter (5-pole, >75 Hz) was applied to each local mfERG response to extract the high frequency components (HFC). The low frequency component (LFC) of each response was represented as the raw response minus the HFC. The amplitude of the HFC was calculated as the root mean square (RMS) for the epoch between 0 and 80 ms of each filtered record. Peak amplitudes for LFC features were quantified as follows: the first negative feature (N1) was calculated as the maximum negative

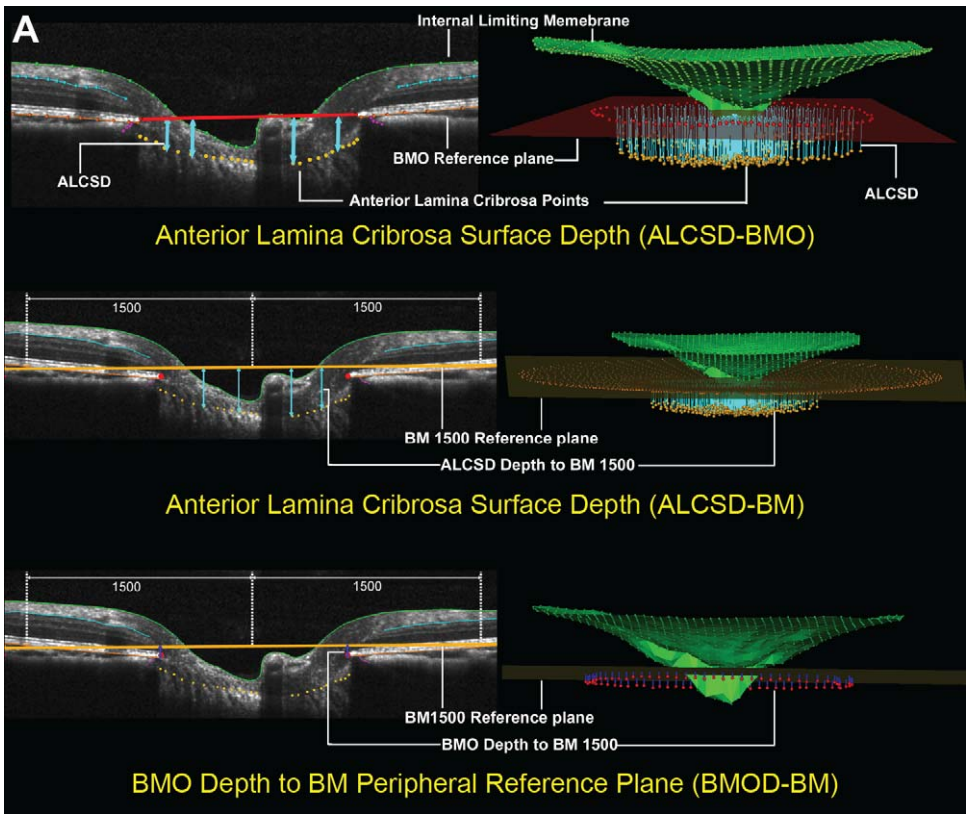

Figure 2. The SDOCT parameters grouped by target tissue. (**A**) ONH connective tissues. SDOCT ONH connective tissue parameters are designed to detect connective tissue deformation (reversible) and/or remodeling (permanent). ALCS depth (*blue arrows*) is measured at each delineated ALCS point as the perpendicular distance from the BMO reference plane (*red line*, *top*) and BM reference plane (*orange line*) defined by two delineated BM points at 1500 μm eccentricity from the BMO centroid (*middle*). BMO Depth is measured at each delineated BMO point as the perpendicular distance from the BM reference plane (*orange line*, *bottom*).

Investigative Ophthalmology & Visual Science

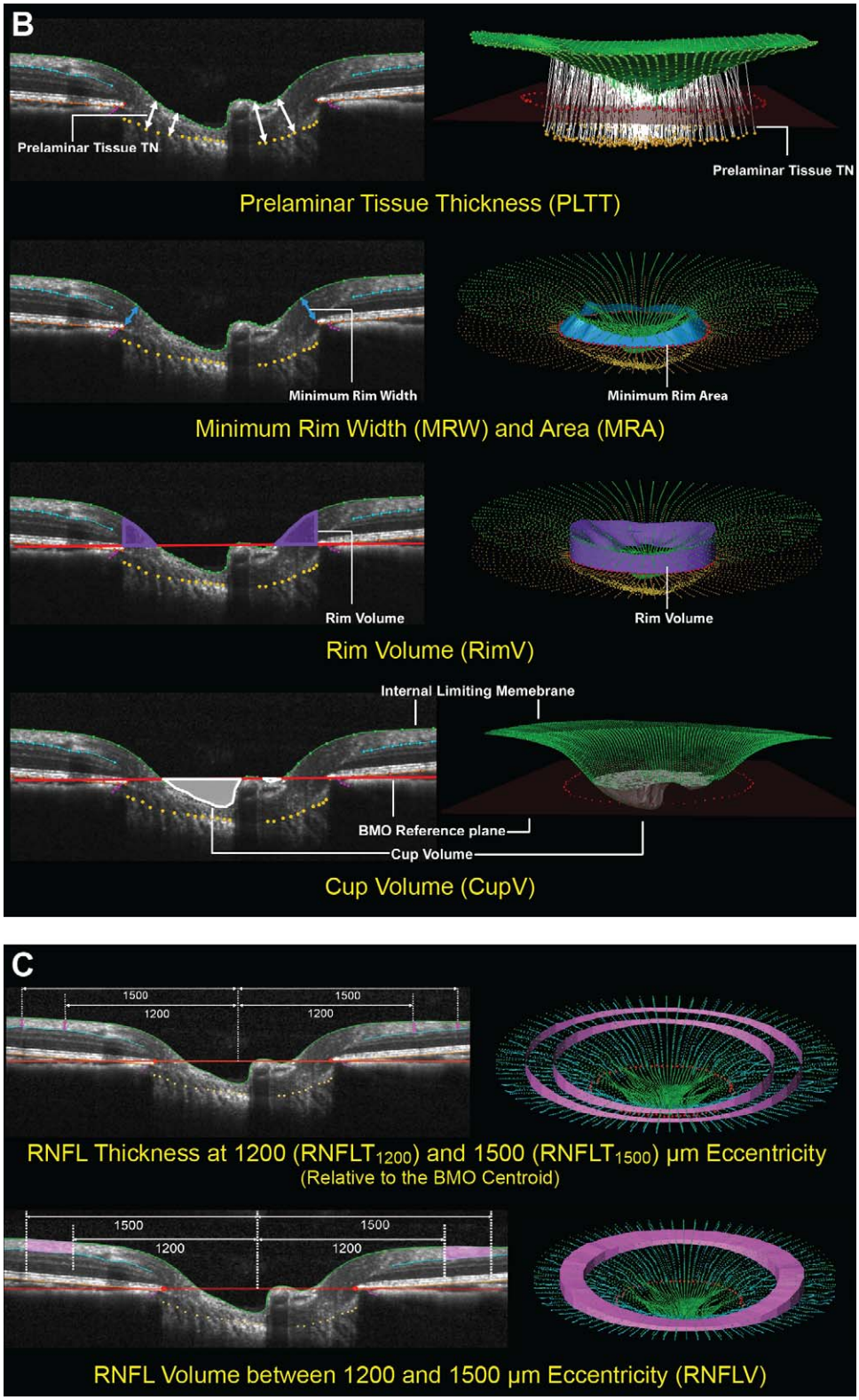

Figure 2. (**B**, **C**) The SDOCT parameters grouped by target tissue (continued). (**B**) ONH neural tissues. Neural tissue parameters are designed to detect neural tissue changes that occur either due to neural tissue damage or secondary to connective tissue deformation. PLTT is measured as the normal from the tangent to the ALCS to the ILM (*green line*, *top*). The MRW (*blue arrows*) is measured at each delineated BMO point (*red*) as the minimum distance to ILM (*upper middle*). When viewed in a 3-D domain, MRW can be translated into minimum rim area (MRA). Rim volume (*purple*) is calculated from the volume bounded by ILM (*green*), BMO reference plane (*red*), and perpendicular line through the BMO (*lower middle*). Cup volume (*grey*) is generated from the volume between ILM B-spline surface and the BMO reference plane (*bottom*). (**C**) Non-standard peripapillary RNFL. $RNFLT_{1200}$ is measured on either side of the posterior RNFL boundary (*turquoise line*) at ILM points that are 1200 µm from the centroid of the 80 delineated BMO points (the BMO centroid). Similarly, $RNFLT_{1500}$ is measured at 1500 µm from the BMO centroid (*top*). The volume between $RNFLT_{1200}$ and $RNFLT_{1500}$ is defined as RNFL volume (*pink*, *bottom*).

Investigative Ophthalmology & Visual Science

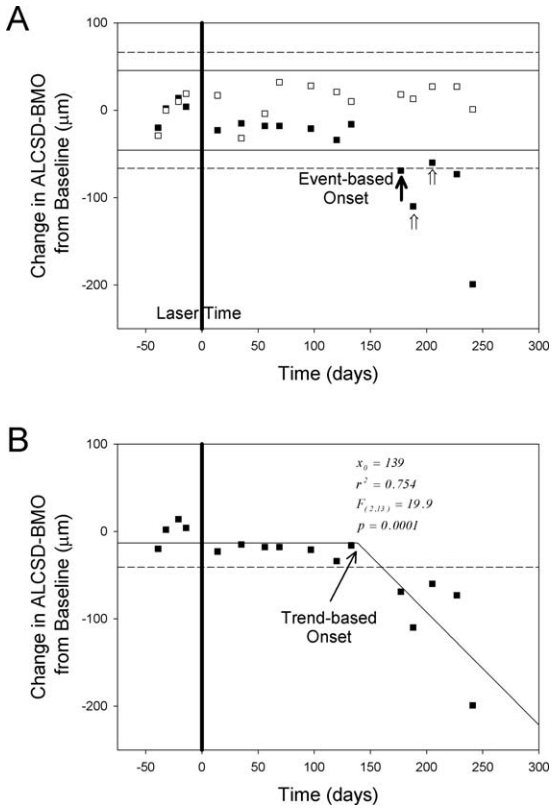

Figure 3. Event-based (**A**) and trend-based (**B**) onset criteria. (**A**) Longitudinal ALCSD-BMO data for eyes of the representative young monkey (Monkey Y3). Changes from mean ALCSD-BMO at baseline (in *vertical axis*) were plotted for the EG (*solid square*) and the contralateral control eye (*open square*) at each imaging session. All data were normalized to the mean baseline value to reflect the changes to baselines. Eye-specific upper and lower 95% CIs for each eye were determined using the baseline testing session and a *t*-distribution (*solid lines* EG eye, *dashed lines* control eye). The number of days in the *x*-axis was normalized to the first day of laser (day 0). Onset of change in either eye (*filled arrow*) was defined to occur at the first post-laser testing session in which the value fell out of the CI, that was confirmed on the next two testing sessions (*open arrows*, onset confirmed ×2). (B) Longitudinal ALCSD-BMO data for EG eyes of the same representative young monkey (Monkey Y3). The trend-based onset ($x_0 = 139$) was determined by the intersection in a segmental fit including one *horizontal* and one *sloped solid lines*. When the fit is statistically different from the mean of ALCSD-BMO data (*horizontal dashed line*, implying no change), the fit and x_0 were considered meaningful and, therefore, was counted as an achieved onset (Methods).

excursion from baseline in the epoch up to 30 ms; the amplitude of the first positivity (P1) was calculated as the voltage difference between the maximum peak and the N1 trough; and the second negativity (N2) was calculated as the difference between baseline and the minima from 30 to 80 ms. The global average (of 37 response locations) for each parameter represented the measurement for each eye at each ERG session.

SLP Parameterization

The GDxVCC measures the relative phase retardance between two beams from a cross-polarized source after a double pass through the tissue sample. By assuming that RNFL thickness is related linearly to retardance, RNFL "thickness" can be converted from retardance measurement after applying a linear conversion factor of 0.67 nm/µm (GDx manual; Carl Zeiss Meditec, Inc.). In this study, we report the global TSNIT average retardance values.

Event and Trend-Based Definitions of Onset (Fig. 3)

For each eye, and for each post-laser imaging session, the average baseline value of each CSLT-MPD, SDOCT, mfERG, and SLP parameter was subtracted from the value at that session to determine the change from baseline. Representative change from baseline data for the SDOCT parameter ALCSD-BMO are presented for both eyes of one monkey in Figure 3. To characterize the timing and frequency of onset detection for each parameter, the event and trend-based criteria were defined as follows.

Event-Based Onset (Fig. 3A)

For each eye and for each parameter, the upper and lower limits of the 95% CI of the baseline data were generated using the Student's *t*-distribution. The onset of change in either direction was identified at the first post-laser testing session in which the value fell out of the CI, followed by confirmation in the two subsequent testing sessions.

Trend-Based Onset (Fig. 3B)

For each eye and for each parameter, onset was defined by the intersection (x_0) of the jointly best-fit segmented linear equations as follows:

$$y = y_0 (if\ x \le x_0)$$

$$y = k(x - x_0) + y_0 (if\ x > x_0).$$

In this segmented linear model, the first segment of the curve described the data without significant changes, while the second segment of the curve described progressive linear change, the rate of which was indicated by the slope k. The intersection of the two segments of the curve, expressed as x_0, was regarded as the onset (Fig. 3B). To determine if this onset was statistically meaningful, the segmented linear model was compared to "no-change" model, which was a best-fit horizontal line with a slope equal to zero. ANOVA was used to compare the two models to see if they were significantly different from each other. $P < 0.05$ validated x_0 as an onset while $P \ge 0.05$ annulled x_0 as an onset.

Survival Analysis to Assess the Relative Performance of Each Parameter

Survival analysis was applied to compare the relative rate and frequency of onset detection among all parameters. The 16 testing parameters were categorized into 4 groups: (1) existing testing modalities (CSLT-MPD, CSLT-TCA, SLP, and mfERG), and three SDOCT groups: (2) ONH-connective tissue (ALCSD-BMO, ALCSD-BM, BMOD-BM, BMOA), (3) ONH-neural tissue (PLTT, MRW, RimV, CupV), and (4) RNFL ($RNFLT_{1200}$, $RNFLT_{1500}$, RNFLV, $RNFLT_{circ}$). One event-based and one trend-based Kaplan-Meier curve was constructed. A logrank test was applied to test for significant differences in the Kaplan-Meier curves generating using each parameter. All analyses were performed in RStudio (RStudio, Inc., Boston, MA).

Investigative Ophthalmology & Visual Science

Table 1. Demographics and IOP Characteristics for Each Study Animal

Animal #	Animal ID	Sex	Age, y	Baseline Mean IOP C/EG, mm Hg	Post-Laser Mean IOP C/EG, mm Hg	Post-Laser Peak IOP C/EG, mm Hg	Cummulative IP Insult-CSLT Onset, mm Hg × Day*	EG Eye Optic Nerve Axon Loss, %†
Y1	25357	M	2.6	10/9	9/11	13/29	309	−29
Y2	25564	F	2.3	8/8	9/13	13/28	183	−19
Y3	26072	F	1.5	5/6	9/10	15/32	61	−15
Y4	26161	F	1.4	6/6	8/11	12/37	17	−4
O1	AM76	F	21.9	9/9	11/16	19/38	80	−12
O2	AM89	M	21.9	11/11	14/16	20/42	94	2
O3	AO23	F	20	9/9	10/18	15/38	649	−13
O4	AP02	F	18.6	7.3/7.3	9/11	13/41	193	−23

Y, young monkeys; O, old monkeys; C, control eyes; EG, experimental glaucoma eyes.
* Cumulative IOP difference between the EG eye and normal eye from the onset of laser treatment to CSLT onset.
† Optic nerve axon loss in the EG eye expressed as percent of its contralateral control eye.

Table 2. Number of Onsets from EG Eye and Control in Event-Based Analysis and Trend-Based Analysis

		Event-Based		Trend-Based	
		EG	Control	EG	Control
Standard testing	CSLT-MPD	4	0	8	1
	CSLT-TCA*	7	3	–	–
	$RNFLT_{circ}$	2	1	5	0
	SLP	1	1	5	0
	mfERG	2	3	1	0
SDOCT ONH	ALCSD-BMO	8	1	8	3
- connective tissues	ALCSD-BM	7	1	8	3
	BMOD-BM	3	1	6	0
	BMOA	0	0	2	0
SDOCT ONH	PLTT	2	0	2	1
- neural tissues	MRW	7	1	7	0
	RimV	7	0	8	0
	CupV	3	0	6	1
Nonstandard SDOCT	$RNFLT_{1200}$	2	1	5	0
- RNFL	$RNFLT_{1500}$	1	1	6	1
	RNFLV	3	2	5	0
Total		59	16	82	10

The onset analysis was performed for each parameter in SDOCT ONH connective tissues, neural tissues, SDOCT RNFL, CSLT, SLP, and mfERG groups.
* Because CSLT-TCA analysis is not quantitative, trend-based onset analysis could not be performed.

Results

Animal Demographics (Table 1)

A total of four young (age, 1.4–2.6 years) and four old (age, 18.6–21.9 years) rhesus monkeys were studied. Each animal was given laser-induced, unilateral chronic IOP elevations of moderate magnitude. Mean post-laser IOP was 11 to 18 mm Hg in the EG eyes and 9 to 14 mm Hg in the control. Maximum post-laser IOP was 18 to 42 mm Hg in the EG eye and 12 to 20 mm Hg in the control eyes. The "cumulative IOP difference" was used to estimate the total post-laser "IOP insult" sustained by each early EG eye as compared to its fellow control eye. It was calculated as IOP difference between the EG eye and the control eye multiplied by the number of days from the last to the current IOP measurement, and summed over the period of post-laser follow-up with the unit "mm Hg × day." Cumulative IOP difference ranged from 50 to 807 (mm Hg × days) at euthanasia. Post-laser time at euthanasia ranged from 139 to 272 days with an average of 202 days. The EG eye RNFL loss ranged from +9.7% (thickening) to −16.8% (thinning), and optic nerve axon loss ranged from +2% to −29%.

Onset Detection by Event-Based Analysis (Table 2)

Among the 16 parameters, only SDOCT ALCSD-BMO detected change onset before euthanasia in all eight EG eyes. SDOCT ALCSD-BM, MRW, RimV, and CSLT TCA each detected onset in seven of eight EG eyes. Among these six parameters, SDOCT RimV detected change onset in zero of eight control eyes, while SDOCT ALCSD-BMO, ALCSD-BM, MRW detected onset in one of eight control eyes, and CSLT TCA detected onset in three of eight control eyes. SDOCT RNFL parameters, SLP, and mfERG detected less frequent change onsets in the EG and control eyes.

Onset Detection by Trend-Based Analysis (Table 2)

SDOCT ALCSD-BMO, ALCSD-BM, RimV, and CSLT MPD detected change onset before euthanasia in all eight EG eyes. SDOCT MRW detected onset in seven of eight EG eyes, and SDOCT BMOD-BM, CupV, and $RNFLT_{1500}$ detected onset in six of eight EG eyes. Among these parameters, SDOCT RimV, MRW, and BMOD-BM detected onset in zero of eight control eyes. SDOCT CupV, $RNFLT_{1500}$, and CSLT MPD detected onset in one of eight control eyes, and ALCSD-BM and ASLCSD-BMO detected onset in three of eight control eyes. SLP and mfERG detected lower levels of change onset in the EG and control eyes. Trend-based analyses of CSLT TCA data were not possible because CSLT-TCA analysis used in this study was not quantitative.

In general, trend-based onsets occurred more frequently in the EG eyes than event-based onsets (82 vs. 59 onsets), but less frequently in the control eyes (10 vs. 16 onsets). Compared to event-based analysis, SDOCT-RNFL and SLP sensitivity improved using trend-based analysis while retaining similar or better specificity.

The Relative Timing and Frequency of Change Onset

Kaplan-Meier curves were plotted for each parameter to compare the relative timing of onset detection by event-based (Fig. 4) and trend-based (Fig. 5) analysis within the eight EG eyes. In both analyses, cumulative onset probability was assessed for each parameter as a function of post-laser time.

In general, for event-based and trend-based analyses, parameters that detected onset most frequently among the EG eyes (Table 1) also detected onset earliest (Figs. 4, 5). Within the event-based analysis (Fig. 4) this is most apparent for SDOCT ALCSD-BMO, ALCSD-BM, MRW, and RimV, and CSLT TCA. Within the trend-based analysis (Fig. 5) this is even more apparent for SDOCT ALCSD-BMO, ALCSD-BM, MRW, and RimV, and CSLT MPD. Interestingly, mfERG within the event-based analysis and SDOCT BMOD-BM within the trend-based survival analysis each detected unusually early onsets in the few eyes in which onset was detected. Among the SDOCT ONH parameters, ALCSD-BMO, ALCSD-BM, MRW, and RimV consistently detected change earlier and in the largest number of eyes. The performance of SDOCT RNFL parameters was enhanced by trend-based analyses, but onset events still were less frequent and later than for the SDOCT and CSLT ONH parameters.

The Kaplan-Meier survival curves for SDOCT ALCSD-BMO, and MRW (from the SDOCT ONH connective and neural tissue groups, respectively) were compared to those from SDOCT $RNFLT_{circ}$, SLP, mfERG, CSLT MPD, and CSLT TCA by Mantel-Cox logrank test (Table 3). For event- and trend-based analyses, the Kaplan-Meier curves for SDOCT ALCSD-BMO and MRW were significantly different from those of SDOCT $RNFLT_{circ}$ and SLP ($P < 0.05$).

Discussion

To date, most longitudinal imaging studies in humans and animals are from CSLT measures of ONH surface change onset,[25,32,33] or OCT or SLP measures of RNFL change onset.[34,35] We reported previously the presence of SDOCT deep ONH change at the time of CSLT ONH surface change onset within the SDOCT data sets of nine rhesus macaque monkeys with chronic, laser-induced, unilateral IOP elevations.[23] In the present report, we hand delineated SDOCT ONH and RNFL anatomy within the baseline and post-laser SDOCT data sets of a second group of four young and four old monkeys carried to a similar CSLT defined endpoint. We then used event-based and trend-based analyses to characterize the relative frequency and timing of SDOCT ONH, SDOCT, and SLP RNFL and mfERG retinal functional change relative to CSLT ONH surface onset. The principal findings of this report are as follows.

First, the conversion from experimental ocular hypertension to glaucomatous damage to the monkey visual system within the EG eyes of these eight animals was detected earliest and most frequently within the ONH neural and deep connective tissues using SDOCT and at the ONH surface using CSLT. This study expanded upon the baseline versus final imaging session analysis of our previous report,[23] by using the full complement of longitudinally acquired data sets in a new group of eight EG eyes. Our data demonstrated that detectable deep and surface ONH change precedes detectable RNFL and retinal functional change in the monkey EG model, and that in six of the eight studied EG eyes these changes occurred at levels of global postmortem orbital optic nerve axon loss (+2 to −29%) that may precede visual field loss.[36] While the lack of detectible change in the RNFLT and retinal function does not mean that pathology is not present, these data supported the notion that very early events in the pathophysiology of glaucoma in the monkey eye occur within the ONH. These data also suggested that events within the RGC axons and soma are either secondary to these ONH events and occur later or, if they are occurring earlier than the ONH events, they are progressing more slowly relative to the sensitivity of the methods used for their detection. These data, therefore, contributed to the growing body of experimental evidence that suggests that the ONH is a primary site of early insult to the visual system in glaucoma.[2,37] In addition, they confirmed that early glaucomatous damage to the monkey ONH includes neural and connective tissue components.[3,38] This finding is important, because it identifies SDOCT-definable endpoints for other experimental models of monkey glaucoma, including primary, chronic, experimental cerebrospinal fluid pressure lowering (Wang N, et al. *IOVS* 2013;54:ARVO E-Abstract 63).

Second, SDOCT ONH neural and connective tissue parameter change preceded or coincided with CSLT ONH surface change in most EG eyes, and demonstrated less frequent change (false positives) among contralateral control eyes. While the frequency of EG eye onset detection of SDOCT ALCSD-BMO and MRW was similar to that of CSLT TCA, TCA detected onset in three of eight control eyes within the event-based analysis. This is consistent with what has been reported in humans in that TCA yielded a low to moderate specificity when the high sensitivity cut-off was chosen.[39,40] CSLT MPD, on the contrary, demonstrated no false-positive onsets based on event-based analysis, but the onset detection in the EG eyes also was lower (50%). SDOCT-based MPD surface characterization has been implemented recently (Zinser G, Heidelberg Engineering GmbH, personal communication, 2013) and will be evaluated in these same data sets in future reports.

Third, several recent reports from Fortune et al.[10,12] have presented evidence that SLP polarimetric change precedes $RNFLT_{circ}$ change in the monkey EG model. In the most recent of these, they found that earlier and more frequent onsets could be detected by SLP measures of RNFL retardance than by SDOCT measures of RNFLT within 41 EG eyes (including the eight reported herein). However, in our study, there was no significant difference in change detection between SLP versus RNFLT by logrank test. Several factors may contribute to this difference in findings. In the current report, the event-based onset definition used eye-specific 95% CIs to mimic current clinical practice and required two subsequent confirmations of onset. The event-based onset analysis in the study of Fortune et al.[12] used calculations of measurement noise to establish the

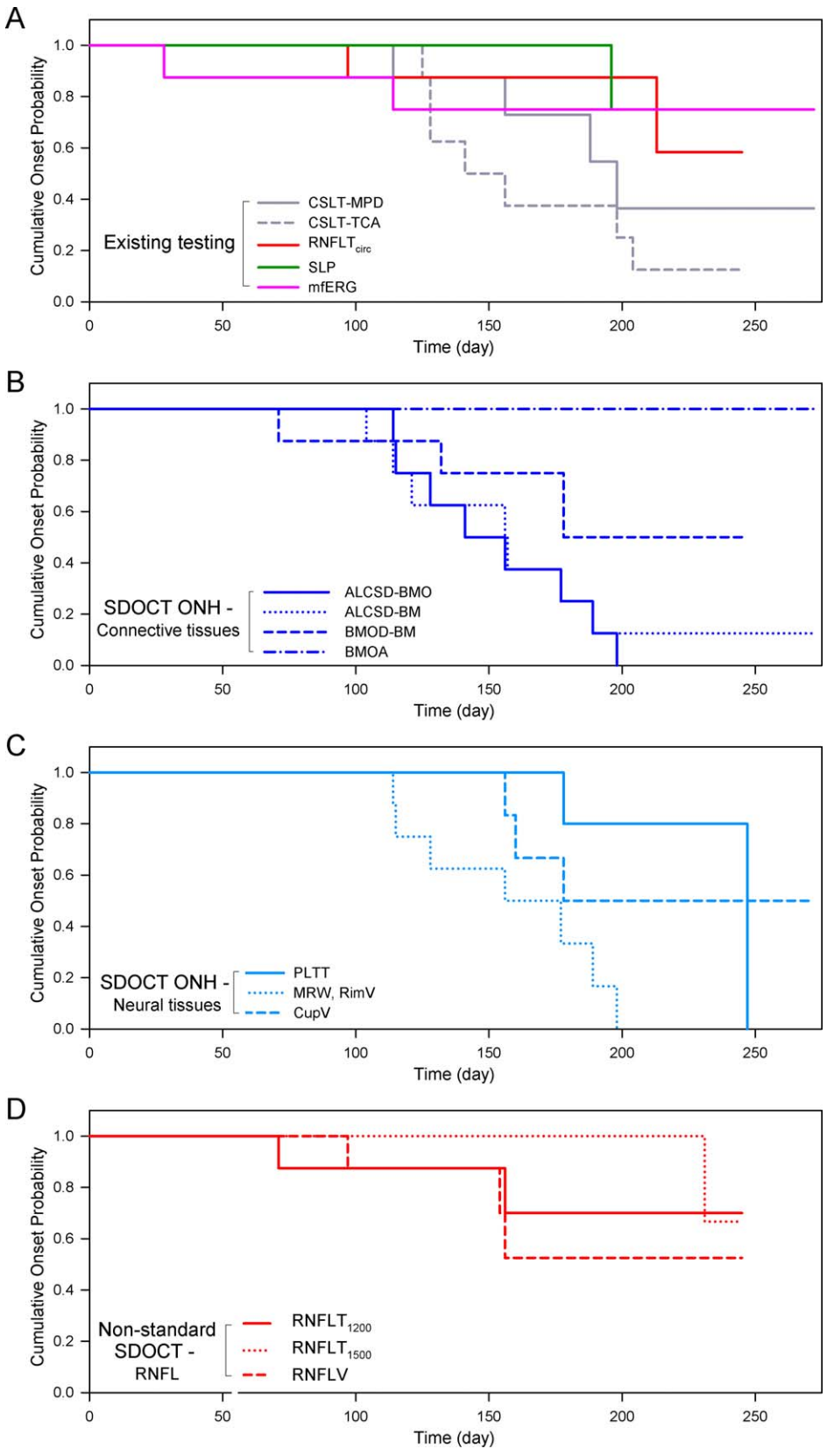

Figure 4. Kaplan-Meier analysis of event-based onset in the eight EG eyes by post-laser time, testing modality, and SDOCT parameter type. (**A**) Existing testing modalities, including CSLT, SLP, and mfERG. (**B**) SDOCT ONH connective tissue parameters. (**C**) SDOCT ONH neural tissue parameters. (**D**) SDOCT RNFL parameters. When compared at similar post-laser days, change detection in the SDOCT ONH parameters ALCSD-BMO and MRW/rim volume, and in the CSLT ONH surface parameters occurred earliest and was most frequent in these eight EG eyes.

Investigative Ophthalmology & Visual Science

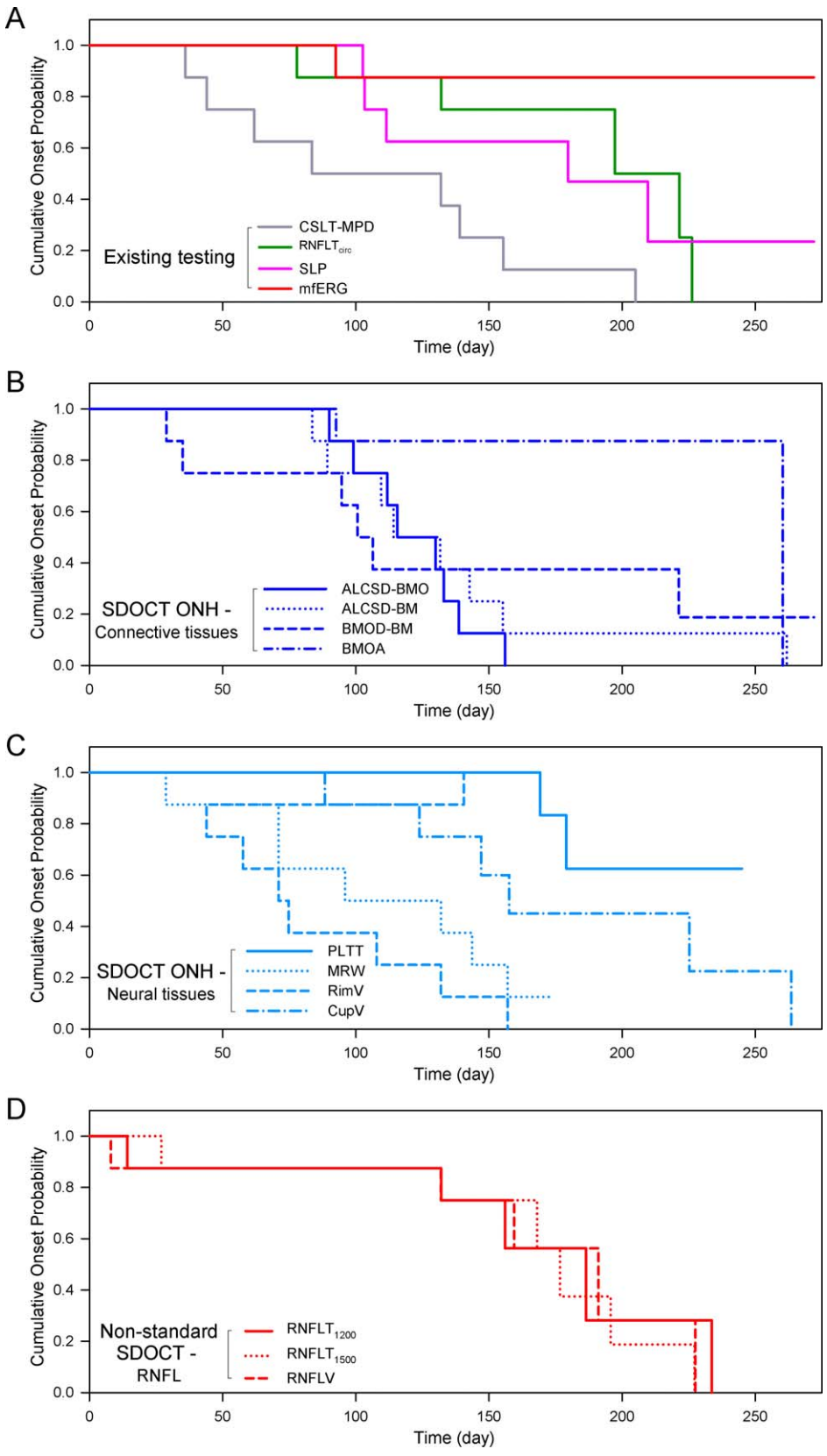

Figure 5. Kaplan-Meier analysis of trend-based onset in the eight EG eyes by post-laser time, testing modality, and SDOCT parameter type. (**A**) Existing testing modalities, including CSLT, SLP, and mfERG. (**B**) SDOCT ONH connective tissue parameters. (**C**) SDOCT ONH neural tissue parameters. (**D**) SDOCT RNFL parameters. Similar to Figure 4, when compared at similar levels of EG eye cumulative IOP insult, change detection in the SDOCT ONH parameters ALCSD-BMO, MRW, and rim volume occurred earliest and was most frequent in these eight EG eyes.

Investigative Ophthalmology & Visual Science

Table 3. *P* Values of Logrank Test for the Comparison of Two Kaplan-Meier Curves by the Existing and SDOCT Parameters (Figs. 4, 5)

Parameter		Standard Testing					SDCOT ONH	
		CSLT–MPD	CSLT–TCA	$RNFLT_{circ}$	SLP	mfERG	ALCSD–BMO	MRW
Standard testing	CSLT–MPD	–	0.252/–	0.755/0.014*	0.373/0.035*	0.899/0.001*	0.049*/0.828	0.109/0.776
	CSLT–TCA†	–	–	0.104/–	0.0378*/–	0.213/–	0.292/–	0.469/–
	$RNFLT_{circ}$	–	–	–	0.544/0.856	0.904/0.057	0.022*/0.006*	0.049*/0.019*
	SLP	–	–	–	–	0.457/0.084	0.005*/0.038*	0.014*/0.049*
	mfERG	–	–	–	–	–	0.087/0.001*	0.161/0.005*
SDOCT ONH	ALCSD–BMO	–	–	–	–	–	–	0.715/0.587
	MRW	–	–	–	–	–	–	–

* In event-based (before the slash) and trend-based (after the slash) onset of the EG eyes, Kaplan-Meier curves in the SDOCT ONH parameters ALCSD-BMO and MRW are consistently and significantly different from the RNFLTcirc and SLP testing modalities ($P < 0.05$).

† Because CSLT-TCA analysis is not quantitative, trend-based onset analysis could not be performed.

95% CIs around baseline variability and found high specificity for endpoint definitions that required only one confirmation. When the onset definition in the current report was changed to a single confirmation of onset, SLP onsets increased to three of eight EG eyes and three of eight control eyes, but the difference in SLP versus RNFLT performance still did not achieve statistical significance. Our findings, therefore, are limited to these eight animals. The ability to detect statistically significant differences in SLP versus RNFL onset detection with the techniques used in this study likely will require a larger numbers of animals, with a greater number carried to later stages of damage as in the previous report.[12]

Fourth, we have previously reported prelaminar tissue thickening at a similar early stage of EG within the postmortem 3D histomorphometric reconstructions of three early EG eyes[41] and a small but statistically significant amount of RNFL thickening in a separate subset of EG eyes.[12] In the present report, only two EG eyes demonstrated longitudinal SDOCT PLTT change by event analysis (one thinned, one thickened). The same changes in the same two eyes were present by trend analysis. While prelaminar tissue thickening was detected in four other EG eyes, it did not achieve statistical significance. The lack of consistent in vivo detection of early prelaminar tissue thickening within the longitudinal SDOCT data of these eight EG eyes suggested that this is not a prominent feature of the conversion from ocular hypertension to early glaucomatous damage. Prelaminar tissue thinning and thickening may have varied conformational components in addition to reflecting aspects of RGC axonal disruption, and loss and/or gliotic changes. Our characterization of SDOCT PLTT may be limited by the accuracy and extent of our delineation of the SDOCT detected, anterior lamina cribrosa surface (see below). Postmortem, 3D histomorphometric assessment of PLTT is underway in the eight animals in this study and may provide additional information about the significance of these findings.

In addition to our principal findings, the following points should be discussed. We and others[16,21,22,23,42,43] have used BMO as a reference plane within 3D histomorphometric and SDOCT ONH data sets. In the current study, parameters using BMO as the reference plane, such as ALCSD-BMO and MRW, performed best in terms of the sensitivity and specificity of glaucomatous onset detection. These data supported the use of BMO as an SDOCT reference plane for change detection early in the neuropathy (i.e., during the transition from ocular hypertension to clinically detectible glaucomatous damage). However, it is possible that the BMO may expand over a long period of time in monkeys with EG[38] and may shift toward the anterior sclera in humans due to progressive thinning of choroid (Rojananuangnit, et al. *IOVS* 2013;54:ARVO E-Abstract 51). In our study, BMO contracted in one and expanded in one EG eye by trend-based analysis (indicated by BMOA), but demonstrated no change using event-based criteria. This is consistent with our previous report in which we found no change in the BMOA in nine monkeys with EG.[27] BMOD-BM (BMO position relative to a more peripheral BM reference plane) deformed posteriorly in three of eight eyes by event-based criteria and six of eight eyes using trend-based analysis. Though we did not obtain longitudinal measurements of choroidal thickness in this study, we interpreted this finding as reflecting a change in the shape of the posterior eye.[23,44] For example, we have suggested previously that more peripheral BM and anterior scleral reference planes may be necessary to sensitively detect outward bowing of the peripapillary sclera in the subset of eyes in which it occurs.[23,37,44] The presence of these findings in the eight EG eyes of our current report supported the importance of peripapillary scleral bowing in the neuropathy, and justify ongoing evaluation of peripheral BM and anterior scleral reference planes as the neuropathy progresses.

Our study has the following limitations. First, only young and very old animals were included, so as to study age-related differences in the clinically detectible onset of glaucoma as part of a larger study. Analysis of these age effects is beyond the scope of our study and will be reported in a separate article that is in preparation. In addition, a follow-up report of parameter performance currently is underway in more than 40 EG eyes of all ages to address these issues specifically.

At the beginning of our study, standard 870-nm SDOCT was the most advanced OCT imaging technique, and enhanced depth imaging[45] and 1050-nm[17] imaging were not yet available. While we have demonstrated histologic validation of 870-nm SDOCT delineation of the anterior laminar surface,[16] the penetration depth of 870-nm SDOCT is not sufficient to visualize the posterior surface of laminar cribrosa in most monkey eyes. Therefore, SDOCT detection of the laminar thickening[21,28] and remodeling[30] that we have described previously in early monkey EG was not possible. Enhanced depth imaging,[28] 1050-nm wavelength acquisition,[17] and enhanced image processing algorithms[46] currently are in place within our laboratory, and may further enhance SDOCT ONH parameter performance.

For a given eye, the relative timing and rate of SDOCT ONH, CSLT ONH surface, SDOCT RNFLT, SLP, and mfERG parameter change may vary depending upon the magnitude and character of the IOP insult. We have reported previously that the rates of ONH and RNFL structural change were most influenced by peak and mean IOP as compared to an independent measure of IOP fluctuation.[24] In these eight monkeys, mean EG eye IOP elevations were modest and peak IOPs were moderate, as intended, although it is unlikely that the true IOP peak occurred at the time it was being measured. The character of parameter change may be different in eyes that are susceptible

to damage at normal levels of IOP or minimal IOP elevations, as well as eyes that are exposed to profound and acute IOP elevations.

CSLT TCA onset for each eye was determined qualitatively by two experienced glaucoma clinicians (masked to the eyes' treatment condition and the results of the other imaging modalities) judging from the longitudinal series of TCA images. No attempt to implement quantitative TCA-based strategies was made, which meant we were not able to evaluate a TCA approach to CSLT ONH surface analysis. Quantification of TCA can be achieved by calculating size of the largest cluster of superpixels within the contour line of the optic disc as described by Nicolela et al.[47] (Artes PH, et al. *IOVS* 2006;47:ARVO E-Abstract 4349). Implementing quantitative TCA analyses within the CSLT data of this study was beyond its scope, but implementation of quantitative TCA approaches to SDOCT ONH surface change detection will be a part of future studies as they become available.

All parameters in this report were calculated on a global basis, which may diminish their ability to detect focal and regional change. In particular, since the ONH blood vessels most commonly shadow the superior and inferior quadrants, the superior and inferior lamina cribrosa (where early change in monkey and human glaucoma is expected) is represented less robustly in our SDOCT ONH connective tissue parameters. This effectively gave more weight to the nasal and temporal quadrants when lamina cribrosa associated parameters were averaged for a global calculation. Regionalization of each structural and functional parameter relative to an anatomically consistent, foveal-BMO nasal temporal axis[15] may change the timing and frequency of change detection by each parameter, and this analysis will be the focus of a follow-up report.

Finally, macular retinal and RGC layer thickness was not imaged in this study, and so change detection within these tissues cannot be compared to the ONH and peripapillary RNFL. Since the completion of this study, SDOCT macular imaging has been added to our protocols. Foveal-BMO acquisition, and analyses of SDOCT ONH, RNFL, and foveal data sets will be included in future comparisons.[15]

In summary, our study used event- and trend-based analyses to longitudinally compare the timing and frequency of SDOCT-detected ONH and RNFLT change to that of SLP and mfERG at the onset of CSLT-detected ONH surface change in the monkey EG model. Our results confirmed the finding of our previous report[12,23,48] that detectable SDOCT deep ONH and CSLT ONH surface change precedes detectable SDOCT RNFLT change in a new group of animals. In addition, they demonstrated that SDOCT deep ONH and CSLT ONH surface change precedes the detection of change by SLP and mfERG. While the SDOCT-detectable neural and connective tissue alterations we describe occurred in the setting of chronic experimental IOP elevation, we propose that they should now serve as targets for the detection of early glaucomatous damage to the monkey ONH regardless of the experimental model (Wang N, et al. *IOVS* 2013;54:ARVO E-Abstract 63). Our data also supported their evaluation in human ocular hypertension.

Acknowledgments

Aspects of this paper were presented at the Annual Meeting of the Association for Research in Vision and Ophthalmology, Fort Lauderdale, Florida, May 1–5, 2011.

Supported by National Institutes of Health Grants R01-EY011610 (CFB), R01-EY022128 (CFB), R01-E019327 (BF); unrestricted research support from Legacy Good Samaritan Foundation, Heidelberg Engineering, Alcon Research Institute, and Sears Medical Trust; and in part by the Department of Health through the award made by the National Institute for Health Research to Moorfields Eye Hospital NHS Foundation Trust and UCL Institute of Ophthalmology for a Biomedical Research Centre for Ophthalmology (NGS). The authors alone are responsible for the content and writing of the paper.

Disclosure: **L. He**, None; **H. Yang**, None; **S.K. Gardiner**, None; **G. Williams**, None; **C. Hardin**, None; **N.G. Strouthidis**, None; **B. Fortune**, Heidelberg Engineering (F); **C.F. Burgoyne**, Heidelberg Engineering (F, R)

References

1. Minckler DS, Bunt AH, Johanson GW. Orthograde and retrograde axoplasmic transport during acute ocular hypertension in the monkey. *Invest Ophthalmol Vis Sci*. 1977;16:426–441.
2. Quigley HA, Addicks EM, Green WR, Maumenee AE. Optic nerve damage in human glaucoma. II. The site of injury and susceptibility to damage. *Arch Ophthalmol*. 1981;99:635–649.
3. Yang H, Downs JC, Bellezza AJ, Thompson H, Burgoyne CF. 3-D histomorphometry of the normal and early glaucomatous monkey optic nerve head: prelaminar neural tissues and cupping. *Invest Ophthalmol Vis Sci*. 2007;48:5068–5084.
4. Bellezza AJ, Rintalan CJ, Thompson HW, Downs JC, Hart RT, Burgoyne CF. Deformation of the lamina cribrosa and anterior scleral canal wall in early experimental glaucoma. *Invest Ophthalmol Vis Sci*. 2003;44:623–637.
5. Burgoyne CF, Varma R, Quigley HA, Vitale S, Pease ME, Lenane PL. Global and regional detection of induced optic disc change by digitized image analysis. *Arch Ophthalmol*. 1994;112:261–268.
6. Heickell AG, Bellezza AJ, Thompson HW, Burgoyne CF. Optic disc surface compliance testing using confocal scanning laser tomography in the normal monkey eye. *J Glaucoma*. 2001;10:369–382.
7. Chauhan BC, Wade BJ, Hamilton DC, LeBlanc RP. Technique for detecting serial topographic changes in optic disc and peripapillary retina using scanning laser tomography. *Invest Ophthalmol Vis Sci*. 2000;41:775–782.
8. Weinreb RN, Zangwill LM, Jain S, et al. Predicting the onset of glaucoma: the confocal scanning laser ophthalmoscopy ancillary study to the Ocular Hypertension Treatment Study. *Ophthalmology*. 2010;117:1674–1683.
9. Tatham AJ, Weinreb RN, Zangwill LM, Liebmann JM, Girkin CA, Medeiros FA. Estimated retinal ganglion cell counts in glaucomatous eyes with localized retinal nerve fiber layer defects. *Am J Ophthalmol*. 2013;156:578–587.
10. Fortune B, Cull G, Burgoyne CF. Relative course of retinal nerve fiber layer birefringence and thickness and retinal function changes after optic nerve transection. *Invest Ophthalmol Vis Sci*. 2008;49:4444–4452.
11. Rangaswamy NV, Zhou W, Harwerth RS, Frishman LJ. Effect of experimental glaucoma in primates on oscillatory potentials of the slow-sequence mfERG. *Invest Ophthalmol Vis Sci*. 2006;47:753–767.
12. Fortune B, Burgoyne CF, Cull GA, Reynaud J, Wang L. Structural and functional abnormalities of retinal ganglion cells measured in vivo at the onset of optic nerve head surface change in experimental glaucoma. *Invest Ophthalmol Vis Sci*. 2012;53:3939–3950.
13. Reis AS, O'Leary N, Yang H, et al. Influence of clinically invisible, but optical coherence tomography detected, optic disc margin anatomy on neuroretinal rim evaluation. *Invest Ophthalmol Vis Sci*. 2012;53:1852–1860.
14. Reis AS, Sharpe GP, Yang H, Nicolela MT, Burgoyne CF, Chauhan BC. Optic disc margin anatomy in glaucoma patients and normal controls with spectral domain optical coherence tomography. *Ophthalmology*. 2012;119:738–747.

15. Chauhan BC, Burgoyne CF. From clinical examination of the optic disc to clinical assessment of the optic nerve head: a paradigm change. *Am J Ophthalmol*. 2013;156:218–227.
16. Strouthidis NG, Grimm J, Williams G, Cull G, Wilson DJ, Burgoyne CF. A comparison of optic nerve head morphology viewed by spectral domain optical coherence tomography and by serial histology. *Invest Ophthalmol Vis Sci*. 2010;51:1464–1474.
17. Srinivasan VJ, Adler DC, Chen Y, et al. Ultrahigh-speed optical coherence tomography for three-dimensional and en face imaging of the retina and optic nerve head. *Invest Ophthalmol Vis Sci*. 2008;49:5103–5110.
18. Chauhan BC, O'Leary N, Almobarak FA, et al. Enhanced detection of open-angle glaucoma with an anatomically accurate optical coherence tomography-derived neuroretinal rim parameter. *Ophthalmology*. 2013;120:535–543.
19. Park HY, Jeon SH, Park CK. Enhanced depth imaging detects lamina cribrosa thickness differences in normal tension glaucoma and primary open-angle glaucoma. *Ophthalmology*. 2012;119:10–20.
20. Quigley HA, Hohman RM. Laser energy levels for trabecular meshwork damage in the primate eye. *Invest Ophthalmol Vis Sci*. 1983;24:1305–1307.
21. Yang H, Downs JC, Girkin C, et al. 3-D histomorphometry of the normal and early glaucomatous monkey optic nerve head: lamina cribrosa and peripapillary scleral position and thickness. *Invest Ophthalmol Vis Sci*. 2007;48:4597–4607.
22. Downs JC, Yang H, Girkin C, et al. 3-D histomorphometry of the normal and early glaucomatous monkey optic nerve head: neural canal and subarachnoid space architecture. *Invest Ophthalmol Vis Sci*.2007;48:3195–3208.
23. Strouthidis NG, Fortune B, Yang H, Sigal IA, Burgoyne CF. Longitudinal change detected by spectral domain optical coherence tomography in the optic nerve head and peripapillary retina in experimental glaucoma. *Invest Ophthalmol Vis Sci*. 2011;52:1206–1219.
24. Gardiner SK, Fortune B, Wang L, Downs JC, Burgoyne CF. Intraocular pressure magnitude and variability as predictors of rates of structural change in non-human primate experimental glaucoma. *Exp Eye Res*. 2012;103:1–8.
25. Burgoyne CF, Mercante DE, Thompson HW. Change detection in regional and volumetric disc parameters using longitudinal confocal scanning laser tomography. *Ophthalmology*. 2002;109:455–466.
26. Chauhan BC, McCormick TA, Nicolela MT, LeBlanc RP. Optic disc and visual field changes in a prospective longitudinal study of patients with glaucoma: comparison of scanning laser tomography with conventional perimetry and optic disc photography. *Arch Ophthalmol*. 2001;119:1492–1499.
27. Reynaud J, Cull G, Wang L, et al. Automated quantification of optic nerve axons in primate glaucomatous and normal eyes–method and comparison to semi-automated manual quantification. *Invest Ophthalmol Vis Sci*. 2012;53:2951–2959.
28. Yang H, Qi J, Hardin C, et al. Spectral-domain optical coherence tomography enhanced depth imaging of the normal and glaucomatous nonhuman primate optic nerve head. *Invest Ophthalmol Vis Sci*. 2012;53:394–405.
29. Povazay B, Hofer B, Hermann B, et al. Minimum distance mapping using three-dimensional optical coherence tomography for glaucoma diagnosis. *J Biomed Opt*. 2007;12:041204.
30. Yang H, Williams G, Downs JC, et al. Posterior (outward) migration of the lamina cribrosa and early cupping in monkey experimental glaucoma. *Invest Ophthalmol Vis Sci*. 2011;52:7109–7121.
31. Chen TC. Spectral domain optical coherence tomography in glaucoma: qualitative and quantitative analysis of the optic nerve head and retinal nerve fiber layer (an AOS thesis). *Trans Am Ophthalmol Soc*. 2009;107:254–281.
32. Artes PH, Chauhan BC. Longitudinal changes in the visual field and optic disc in glaucoma. *Prog Retin Eye Res*. 2005;24:333–354.
33. Medeiros FA, Lisboa R, Zangwill LM, et al. Evaluation of progressive neuroretinal rim loss as a surrogate end point for development of visual field loss in glaucoma [published online ahead of print August 12, 2013]. *Ophthalmology*. doi:10.1016/j.ophtha.2013.06.026.
34. Alencar LM, Zangwill LM, Weinreb RN, et al. Agreement for detecting glaucoma progression with the GDx guided progression analysis, automated perimetry, and optic disc photography. *Ophthalmology*. 2010;117:462–470.
35. Wollstein G, Schuman JS, Price LL, et al. Optical coherence tomography longitudinal evaluation of retinal nerve fiber layer thickness in glaucoma. *Arch Ophthalmol*. 2005;123:464–470.
36. Harwerth RS, Vilupuru AS, Rangaswamy NV, Smith EL III. The relationship between nerve fiber layer and perimetry measurements. *Invest Ophthalmol Vis Sci*. 2007;48:763–773.
37. Burgoyne CF. A biomechanical paradigm for axonal insult within the optic nerve head in aging and glaucoma. *Exp Eye Res*. 2011;93:120–132.
38. Yang H, Downs JC, Burgoyne CF. Physiologic intereye differences in monkey optic nerve head architecture and their relation to changes in early experimental glaucoma. *Invest Ophthalmol Vis Sci*. 2009;50:224–234.
39. Bowd C, Balasubramanian M, Weinreb RN, et al. Performance of confocal scanning laser tomograph topographic change analysis (TCA) for assessing glaucomatous progression. *Invest Ophthalmol Vis Sci*. 2009;50:691–701.
40. O'Leary N, Crabb DP, Mansberger SL, et al. Glaucomatous progression in series of stereoscopic photographs and Heidelberg retina tomograph images. *Arch Ophthalmol*. 2010;128:560–568.
41. Yang H, Thompson H, Roberts MD, Sigal IA, Downs JC, Burgoyne CF. Deformation of the early glaucomatous monkey optic nerve head connective tissue after acute IOP elevation in 3-D histomorphometric reconstructions. *Invest Ophthalmol Vis Sci*. 2011;52:345–363.
42. Yan DB, Coloma FM, Metheetrairut A, Trope GE, Heathcote JG, Ethier CR. Deformation of the lamina cribrosa by elevated intraocular pressure. *Br J Ophthalmol*. 1994;78:643–648.
43. Strouthidis NG, Yang H, Downs JC, Burgoyne CF. Comparison of clinical and three-dimensional histomorphometric optic disc margin anatomy. *Invest Ophthalmol Vis Sci*. 2009;50:2165–2174.
44. Strouthidis NG, Fortune B, Yang H, Sigal IA, Burgoyne CF. Effect of acute intraocular pressure elevation on the monkey optic nerve head as detected by spectral domain optical coherence tomography. *Invest Ophthalmol Vis Sci*. 2011;52:9431–9437.
45. Spaide RF. Enhanced depth imaging optical coherence tomography of retinal pigment epithelial detachment in age-related macular degeneration. *Am J Ophthalmol*. 2009;147:644–652.
46. Mari JM, Strouthidis NG, Park SC, Girard MJ. Enhancement of lamina cribrosa visibility in optical coherence tomography images using adaptive compensation. *Invest Ophthalmol Vis Sci*. 2013;54:2238–2247.
47. Nicolela MT, Soares AS, Carrillo MM, Chauhan BC, LeBlanc RP, Artes PH. Effect of moderate intraocular pressure changes on topographic measurements with confocal scanning laser tomography in patients with glaucoma. *Arch Ophthalmol*. 2006;124:633–640.
48. Fortune B, Reynaud J, Wang L, Burgoyne CF. Does optic nerve head surface topography change prior to loss of retinal nerve fiber layer thickness: a test of the site of injury hypothesis in experimental glaucoma. *PLoS One*. 2013;8:e77831.

Investigative Ophthalmology & Visual Science